aerospace

MDPI

Article

Real Gas Effects on Receptivity to Roughness in Hypersonic Swept Blunt Flat-Plate Boundary Layers

Yanxin Yin [1,2], Ruiyang Lu [1], Jianxin Liu [3,4,*] and Zhangfeng Huang [1]

[1] Department of Mechanics, Tianjin University, Tianjin 300072, China; xinye624@163.com (Y.Y.); lu_ruiyang@163.com (R.L.); hzf@tju.edu.cn (Z.H.)
[2] Beijing Institute of Astronautical Systems Engineering, Beijing 100076, China
[3] State Key Laboratory of Aerodynamics, Mianyang 621000, China
[4] Lab of High-Speed Aerodynamics, Tianjin University, Tianjin 300072, China
* Correspondence: shookware@tju.edu.cn

Abstract: Temperatures within the boundary layers of high-enthalpy hypersonic flows can soar to thousands or even tens of thousands of degrees, leading to significant real gas phenomena. Although there has been significant research on real gas effects on hypersonic boundary layer stability, their impact on the boundary layer's receptive stage is still poorly understood. Most aerodynamic boundary layers in flight vehicles are three-dimensional. Because of complex geometry and significant crossflow effects, the crossflow mode in three-dimensional boundary layers is crucial in hypersonic vehicle design. In this study, a linear stability analysis (LST) accounting for chemical nonequilibrium effects (CNE) and its adjoint form (ALST) is developed to investigate the real gas effects on the stability and receptivity of stationary crossflow modes. The results indicate that real gas effects significantly influence the receptivity of stationary crossflow modes. Specifically, chemical nonequilibrium effects destabilize the crossflow modes but reduce the receptivity coefficients of the stationary crossflow modes. The Mach number effect was also investigated. It was found that increasing the Mach number stabilizes the stationary crossflow modes, but the receptivity coefficients increase. As the Mach number progressively rises, these effects alternately dominate, leading to a non-monotonic shift in the transition position.

Keywords: hypersonic boundary layer; reacting flow; linear stability analysis

Citation: Yin, Y.; Lu, R.; Liu, J.; Huang, Z. Real Gas Effects on Receptivity to Roughness in Hypersonic Swept Blunt Flat-Plate Boundary Layers. *Aerospace* **2024**, *11*, 58. https://doi.org/10.3390/aerospace11010058

Academic Editor: Sergey Leonov

Received: 8 November 2023
Revised: 28 December 2023
Accepted: 5 January 2024
Published: 7 January 2024

1. Introduction

The laminar-to-turbulent transition in hypersonic flows is vital for aerodynamic and aerothermal vehicle design because it is accompanied by a significant increase in skin friction and heat transfer. Nevertheless, accurately predicting the transition position remains exceedingly challenging, as this process is markedly influenced by external factors such as noise and turbulence levels and wall roughness. Morkovin [1] systematically summarized the potential existence of multiple boundary layer development transition pathways, with the natural transition process being the most probable in actual flight conditions. Generally, the natural transition process can be divided into four stages: receptivity, linear instability, nonlinear instability, and turbulence.

As the first transition stage, receptivity is the process by which external disturbances excite mode disturbances within the boundary layer. These external disturbances can arise from freestream or localized surface imperfections. Receptivity can be classified into natural and forced receptivity based on different external disturbance types. Exploring the receptivity process is fundamentally directed at elucidating the "scale conversion" relationship between external and mode disturbances within the boundary layer.

For natural receptivity, external disturbances can be acoustic, entropy, and vorticity waves. Goldstein [2] computed receptivity coefficients for acoustic waves at a zero incidence angle for a flat-plate boundary layer, while Kerschen [3] investigated the receptivity of

vorticity waves to mode disturbances within the boundary layer. Hammerton's [4,5] works extended and applied the receptivity theory from flat plates to parabolic leading edges. Notably, these studies primarily centered around subsonic flow. However, the boundary layer's strong compressibility introduces new receptivity mechanisms for hypersonic flows. The best known is the mode synchronization theory proposed by Fedorov [6], suggesting two disturbance mode synchronizations, near the leading edge and at a location downstream, which completely excite the most unstable Mack mode. This theory has been confirmed by a direct numerical simulation conducted by Zhong [7].

Unlike natural receptivity, forced receptivity involves directly exciting instability modes through wall surface actions like periodic blowing–suction, local temperature changes, and wall roughness. Theoretical studies have found that even very small localized imperfections can trigger significant local receptivity, so this mechanism is important. The "finite Reynolds number theory" developed by Goldstein [8–10] is well-known in forced receptivity research, and relevant studies can be carried out using this theory whether the wall disturbance excitation is isolated or distributed.

In the hypersonic boundary layer context, Ruban [11] studied steady longitudinal vortex excitation using spectral methods, while Duan [12] explored forced receptivity over flat-plate boundary layers using direct numerical simulation. Beyond the "finite Reynolds number theory" and direct numerical simulations, a practical compromise involves solving adjoint equations. This method offers computational efficiency and mathematical rigor, making it accessible to a wider audience. Based on this approach, Tempelmann [13] examined crossflow mode receptivity on a subsonic swept wing driven by roughness. Wang [14] investigated plasma actuation's receptivity at the wall, and Xi [15] explored the stability and receptivity of a swept blunt body.

In addition, the friction between the vehicle surface and the air generates elevated temperatures as freestream Mach numbers increase, reaching into the range of thousands or even tens of thousands of degrees within the boundary layer. This region experiences various thermal and chemical processes, causing significant real gas effects, and the traditional assumption of a calorically perfect gas (CPG) fails. To capture the flow's attributes with precision, researchers have employed a variety of gas models, including the thermally perfect gas (TPG) model accounting for vibrational energy excitation, the chemical nonequilibrium (CNE) gas model, the thermochemical nonequilibrium (TCNE) gas model, and the thermochemical equilibrium (TCE) gas model, assuming both thermal and chemical equilibrium states are achieved [16].

Over the past two decades, numerous studies have focused on the real gas effect implications on flow stability. Malik [17,18] investigated the impact of dissociation effects on flow stability using a self-similar solution of a flat-plate boundary layer for a thermochemical equilibrium gas. They discovered that the growth rate of the second mode was higher with the chemical equilibrium model, and the range of unstable frequencies shifted toward lower frequencies. Stuckert [19,20] conducted a similar study on the boundary layer using a chemical nonequilibrium model considering finite chemical reaction rates. Their findings suggested that heat absorption through chemical reactions expands the supersonic region within the boundary layer, reducing the second mode's frequency.

Both thermochemical and various thermodynamic and transport models can significantly impact flow stability [21–25]. Miró Miró [25] systematically compared the effects of these models on flow stability. In addition to the commonly observed second mode, supersonic modes in high-temperature boundary layers have garnered considerable attention [26–28]. In calorically perfect gas cases, supersonic modes are limited to extremely cold wall conditions. However, considering real gas effects appears to facilitate the occurrence of supersonic modes. Research indicates that significant nose bluntness can elevate the instability of the supersonic mode even beyond the second mode, making it the dominant mode [28]. While most prior studies focused on the linear growth stage of disturbances, recent research has considered the nonlinear stage, exploring the impact of

real gas effects using methods like direct numerical simulation (DNS) [29] and nonlinear parabolized stability equations (NPSE) [30,31].

There has been extensive research on real gas effects on the growth stage of disturbances. However, few studies have focused on the impact of a real gas on the receptivity stage. To accurately predict the transition position, it is crucial to consider not only the growth stage but also the initial amplitude of the disturbance, which is an essential factor influencing the transition position. In the case of blunt body swept flows, the dominant unstable mode is the crossflow mode, which can be categorized into two classical types: traveling and stationary modes, based on their frequencies. The former is associated with the interaction of freestream disturbances and wall roughness, while the latter is only related to wall roughness. These make the receptivity coefficient of a stationary mode significantly larger than that of a traveling mode. As a result, the stationary mode is typically more critical than the traveling mode because it has a significantly larger receptivity amplitude.

This research on the effect of the real gas on the receptivity of hypersonic stationary crossflow modes to roughness is the primary focus. This paper is structured as follows: Section 2 introduces the governing equations and methodologies for solving for the base flow, stability, and receptivity. Section 3 examines the influence of real gas effects and the Mach number on the stability and receptivity of stationary crossflow modes and provides predictions for transition positions. Finally, the conclusions from this study are presented in Section 4.

2. Mathematical Descriptions

2.1. Physical Model

The physical model used in this paper is a swept blunt flat plate with a nose bluntness of 35 mm, a wall temperature T_w = 700 K, and a swept angle of 45° (Figure 1). The freestream parameters are shown in Table 1, where CPG is the calorically perfect gas model, and CNE is the chemical nonequilibrium gas model. Five Mach numbers ranging from 10 to 20 were computed.

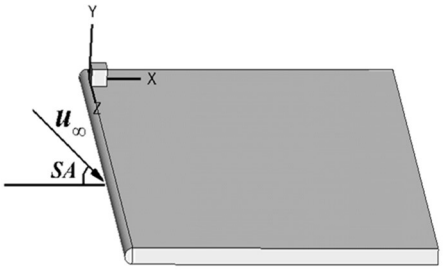

Figure 1. Swept Blunt Flat-plate model.

Table 1. Freestream conditions and the gas models.

Ma	Altitude (km)	T_∞ (K)	Gas Models
10, 12, 15, 17, 20	30	226.5	CPG, CNE

2.2. Governing Equations

The base flow is determined by solving the Navier–Stokes equations, considering finite chemical reaction rates. Both 5-species (N_2, O_2, NO, O, N) and 11-species (N_2, O_2, NO, O, N, NO^+, e^-, O^+, N^+, O_2^+, N_2^+) air reaction models were used in this paper, and the specific chemical reactions are given in Appendix A. The governing equations for the reacting flow with N_s species encompass three momentum equations, N_s continuity equations, and an energy equation,

$$\begin{gathered}\frac{\partial \rho}{\partial t}+\nabla\cdot(\rho\vec{u})=0\\ \frac{\partial \rho\vec{u}}{\partial t}+\nabla\cdot(\rho\vec{u}\vec{u})+\nabla p=0\\ \frac{\partial \rho_i}{\partial t}+\nabla\cdot(\rho_i\vec{u})=\nabla\cdot(\lambda_i\nabla c_i)+w_{s,i}\ ,\ i\in(2,\ N_s)\\ \frac{\partial \rho E}{\partial t}+\nabla\cdot\left[(\rho E+p)\vec{u}\right]=\nabla\cdot(k\nabla T)+\sum_{i=1}^{N_s}\nabla\cdot(\lambda_i h_i\nabla c_i)+\nabla(u\cdot\tau)\end{gathered} \tag{1}$$

where ρ, $\vec{u}$, p and T are the density, velocity, pressure, and temperature of the gas, respectively, and ρ_i, λ_i, c_i, h_i and $w_{s,i}$ are the density, diffusion coefficient, mass fraction, specific enthalpy, and mass source term due to chemical reaction of species i, respectively. k is the heat conductivity, μ is the dynamic viscosity, E is total internal energy, and τ is the viscous stress, defined as

$$\tau=\mu\left(\nabla\vec{u}+\left(\nabla\vec{u}\right)^T\right)-\frac{2}{3}\mu(\nabla\cdot\vec{u})\boldsymbol{I} \tag{2}$$

The governing equations can be derived for the calorically perfect gas by eliminating the species continuity equations from Equation (1) and considering all diffusion-related terms negligible. The coefficients k and μ are determined utilizing Sutherland's law, while the total energy E is computed based on a constant specific gas ratio,

$$E=\frac{p}{\rho(\gamma-1)}+\frac{1}{2}(\vec{u}\cdot\vec{u}^T) \tag{3}$$

For mixed gases, the parameters ρ, p, and E and the transport properties μ and k are related to the individual species, which continue to satisfy their respective ideal gas equations of state. The pressure of the mixture can be determined using Dalton's law of partial pressures. The thermodynamic relationships between the gas mixture and its constituent species are

$$c_i=\frac{\rho_i}{\rho},\ \rho=\sum_{i=1}^{N_s}\rho_i,\ p=\rho T\sum_{i=1}^{N_s}c_iR_i,\ E=\sum_{i=1}^{N_s}c_ih_i+\frac{1}{2}(\vec{u}\cdot\vec{u}^T)-\frac{p}{\rho} \tag{4}$$

where R_i is the specific gas constant for species i. No universally accepted set of accurate models currently exists for high-temperature mixed gases despite the development of various thermodynamic models by researchers. A widely used thermodynamic model for the species' heat capacities and enthalpies is the curve fits given by Gupta in 1990 [32],

$$\frac{M_ih_i}{R_0T}=a_1+\frac{1}{2}a_2T+\frac{1}{3}a_3T^2+\frac{1}{4}a_4T^3+\frac{1}{5}a_6T^4+\frac{a_6}{T} \tag{5}$$

where a_1 to a_7 are the fitting coefficients, and M_i is the molar mass of species i.

Various transport models can be used to calculate the transport coefficients of mixed gases. The most accurate transport model is the CE model (Chapman and Enskog's molecular theory of gases), but this model is computationally intensive and difficult to apply to stability analyses. In this paper, the curve fits given by Gupta and Yos [33] in 1990 were used to calculate each species' viscosity and heat conductivity. This is one of the most common viscosity and thermal conductivity models used in hypersonic stability studies,

$$\begin{gathered}ln\mu_i=A_{\mu_i}(lnT)^2+B_{\mu_i}lnT+C_{\mu_i}\\ lnk_i=A_{k_i}(lnT)^4+B_{k_i}(lnT)^3+C_{k_i}(lnT)^2+D_{k_i}lnT+E_{k_i}\end{gathered} \tag{6}$$

where $A_{\mu i}$, $B_{\mu i}$, $C_{\mu i}$, A_{ki}, B_{ki}, C_{ki}, D_{ki}, and E_{ki} are the fitting coefficients. Wilke's mixing rule gives the transport coefficients of the mixed gases,

$$\mu = \sum_{i=1}^{N_s} \frac{x_i \mu_i}{\sum_{j=1}^{N_s} x_j \phi_{ij}}, \; k = \sum_{i=1}^{N_s} \frac{x_i k_i}{\sum_{j=1}^{N_s} x_j \phi_{ij}}, \; \phi_{ij} = \frac{1}{\sqrt{8}} \left(1 + \frac{M_i}{M_j}\right)^{-1/2} \left[1 + \left(\frac{\mu_i}{\mu_j}\right)^{1/2} \left(\frac{M_i}{M_j}\right)^{1/4}\right]^2 \tag{7}$$

First, the flat-plate boundary layer flow with Ma = 10 was calculated using the five-species air model, which does not consider ionization. The temperature and velocity profiles within the boundary layer agree well with the results from Ref. [25], as shown in Figure 2a. The RAM-C with Ma = 28.3 was calculated using the 11-species air ionization model. Figure 2b displays the maximum electron number density distribution along the *x*-axis for RAM-C, along with the computational results of Ref. [23] and the experimental results [24]. The results obtained in this study agree well with the reference results, demonstrating the base flow solver's reliability.

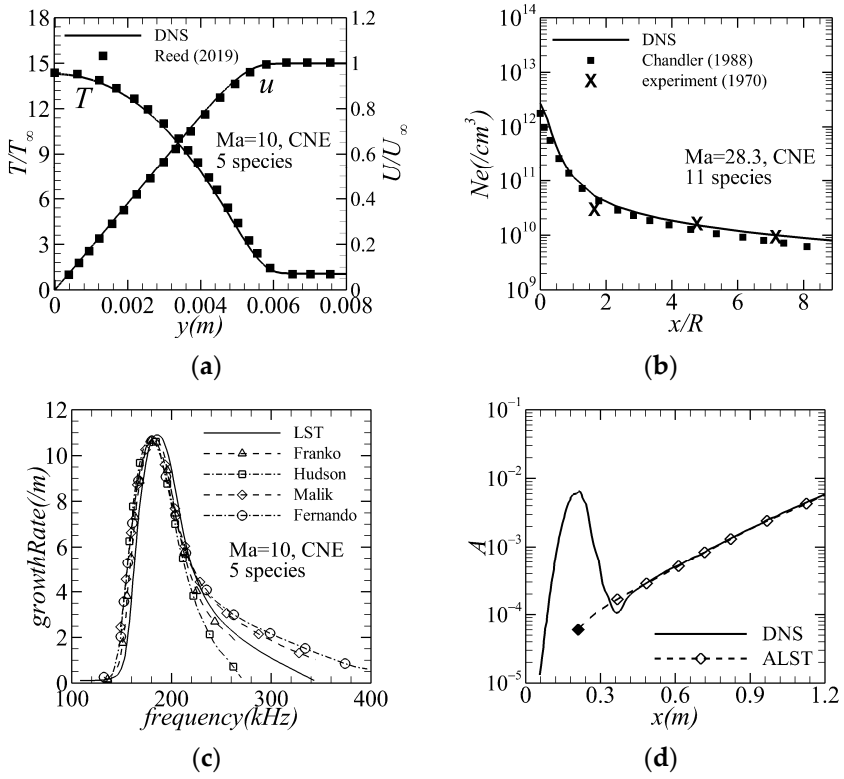

Figure 2. Comparison between present results and those of the references [22–25]: (**a**) Baseflow profile, (**b**) The maximum electron density distribution along *x*-axis for RAM-C, (**c**) Growth rate of the second mode, and (**d**) Disturbance amplitude evolution.

2.3. Linear Stability Analysis (LST) and Their Adjoint (ALST)

The instantaneous flow is first decomposed into mean and perturbed components,

$$\phi = \phi_0 + \phi' \tag{8}$$

For chemically nonequilibrium flows, $\phi = \left[\rho, \vec{u}, T, c_i\right]$, $s \in [2,5]$. The linear disturbance equation can be derived by incorporating Equation (8) into Equation (1), eliminating the equations satisfied by the base flow and disregarding the nonlinear terms. In the quasi-parallel linear stability theory (LST) approximation, the solution of the linearized disturbance equations is considered in the form of normal modes,

$$\phi' = \hat{\phi}(y) e^{i(\alpha x + \beta z - \omega t)} + c.c \tag{9}$$

where α, β, and ω are the streamwise wavenumber, spanwise wavenumber, and frequency, respectively, and *c.c* is the complex conjugate. Substituting Equation (9) into the linear disturbance equations, the full eigen-equation of the spatial modes can be recast as

$$L\hat{\phi} = \left(L_2\alpha^2 + L_1\alpha + L_0\right)\hat{\phi} = 0 \tag{10}$$

where $\hat{\phi}$ is the eigenfunction. For the spatial model, ω is a real number, α and β are complex numbers, and -α_i is the flow growth rate, usually denoted as σ.

Building upon the LST equations, the adjoint equations' derivation necessitates defining the inner product. Given that the domain of definition of the LST equation is oriented in the y-direction, the inner product can be defined as

$$\langle \phi, \psi \rangle = \int_0^\infty \overline{\psi}\phi dy \tag{11}$$

According to the definition of the adjoint operator, $\left\langle L\hat{\phi}, \hat{\phi}^* \right\rangle = \left\langle \hat{\phi}, L^*\hat{\phi}^* \right\rangle$, where L^* is the adjoint equation operator and $\hat{\phi}^*$ is the adjoint eigenfunction. The adjoint LST (ALST) equation can be written as

$$L^*\hat{\phi}^* = \left({L_2}^*\alpha^2 + {L_1}^*\alpha + {L_0}^*\right)\hat{\phi}^* \tag{12}$$

Imposing a homogeneous boundary condition for the adjoint vector, one can obtain the following orthogonality relation based on the definition of the inner product,

$$\begin{cases} \left\langle \hat{\phi}_\alpha^*, [L_1 + (\alpha + \alpha_s)L_2]\hat{\phi}_{\alpha_s} \right\rangle = 0, \ \alpha \neq \alpha_s \\ \left\langle \hat{\phi}_\alpha^*, [L_1 + (\alpha + \alpha_s)L_2]\hat{\phi}_{\alpha_s} \right\rangle = Q, \ \alpha = \alpha_s \end{cases} \tag{13}$$

The solution of the linearized disturbance equations can be expanded into the normal modes of continuous and discrete spectra,

$$A_0(x, y, \beta, \omega) = \sum_j \int_0^\infty C_j(k)\hat{\phi}_{\alpha_j(k)}(y)e^{i\alpha_j(k)x}dk + \sum_m C_m\hat{\phi}_{\alpha_m}(y)e^{i\alpha_m x} \tag{14}$$

With the help of the above orthogonality relation, Equation (13), one can find the amplitude of a mode to the formal solution,

$$Ce^{i\alpha x} = \frac{\left\langle \hat{\phi}_\alpha^*, (L_1 + 2\alpha L_2)A_0 \right\rangle}{Q} \tag{15}$$

Forming the inner product between $\hat{\phi}_s$ and the inhomogeneous LST equation, the detailed derivation of the receptivity coefficients is given as

$$\begin{gathered} \left\langle \hat{\phi}_\alpha^*, \left(L_0 + \alpha_s L_1 + \alpha_s^2 L_2\right)\hat{\phi}_{\alpha_s}^* - \hat{S} \right\rangle = \\ \left\langle \left(L_0^* + \overline{\alpha}L_1^* + \overline{\alpha}^2 L_2^*\right)\hat{\phi}_\alpha^*, \hat{\phi}_{\alpha_2} \right\rangle + B.C. - \left\langle \hat{\phi}_\alpha^*, \hat{S} \right\rangle + \left\langle \hat{\phi}_\alpha^*, (\alpha_s - \alpha)[L_1 + (\alpha_s + \alpha)L_2]\hat{\phi}_{\alpha_s} \right\rangle \end{gathered} \tag{16}$$

The first term equals zero with the definition of the adjoint equation. The second and third terms represent the forcing from inhomogeneous boundary conditions and the sources, respectively. Among them, the bilinear concomitant boundary condition *(B.C.)* is expressed explicitly as

$$B.C. = \overline{\rho}_w\hat{\rho}_w^*\hat{v}_w + \frac{\overline{\mu}}{Re_0}\frac{\partial\hat{u}_w^*}{\partial y}\hat{u}_w + \frac{3\overline{\mu}}{4Re_0}\frac{\partial\hat{v}_w^*}{\partial y}\hat{v}_w + \frac{\overline{\mu}}{Re_0}\frac{\partial\hat{w}_w^*}{\partial y}\hat{w}_w + \frac{\overline{\mu}}{Re_0 Pr}\frac{\partial\hat{T}_w^*}{\partial y}\hat{T}_w \tag{17}$$

Based on the orthogonality relation Equation (13) and utilizing Equations (14) and (15), the following identity is determined,

$$Ce^{i\alpha x} = \frac{1}{2\pi Q}\int_{-\infty}^{\infty} \frac{\langle \hat{\phi}_\alpha^*, \hat{S}\rangle - B.C.}{\langle \alpha_s - \alpha\rangle e^{i\alpha_s x} d\alpha_s} \tag{18}$$

and the receptivity coefficient can be found as the residue value at the pole $\alpha = \alpha_s$,

$$C = i\frac{\langle \hat{\phi}_\alpha^*, \hat{S}\rangle - B.C.}{Q} \tag{19}$$

The aforementioned method for computing the receptivity coefficient is called the adjoint LST (ALST) [14]. The evolution of the disturbance excited by surface imperfections can be obtained by taking the receptivity coefficient C as the initial disturbance amplitude. Figure 2c shows the growth rate calculated using the LST, and Figure 2d shows the amplitude evolution obtained by the ALST and DNS. Their agreement validates the accuracy of the stability and receptivity programs used in this study.

3. Results and Discussion

3.1. Baseflow and Linear Stability Analysis

In this paper, the maximum Mach number is 20, but the maximum streamwise velocity component u is limited to about 4200 m/s due to the sweep angle. We calculated the Ma = 20 case using two air reaction models, 5-species and 11-species. It was found that the ionization reaction has not yet occurred at this time, and the flow fields obtained under the two models largely overlap. Therefore, the 5-species air reaction model was chosen for subsequent calculations, which is appropriate for the cases examined in this paper.

Figure 3 shows the temperature distributions around the nose region at different Mach numbers, highlighting the significant impact of the chemical nonequilibrium effect on the flow field characteristics. The endothermic chemical reaction significantly reduces the temperature near the stagnation point and decreases the shock stand-off distance. Figure 4 shows the oxygen/nitrogen mass fraction distribution around the nose. The series of chemical reactions in the air have not yet occurred when the temperature is below 2500 K. It can be seen that when Ma = 10, most of the flow field remains chemically frozen. The results of the chemical nonequilibrium model exhibit only slight deviations from the calorically perfect gas model in this case. As the Mach number increases, chemical reactions occur, with oxygen dissociating initially. At Ma = 20, oxygen undergoes nearly complete dissociation, while nitrogen begins to dissociate.

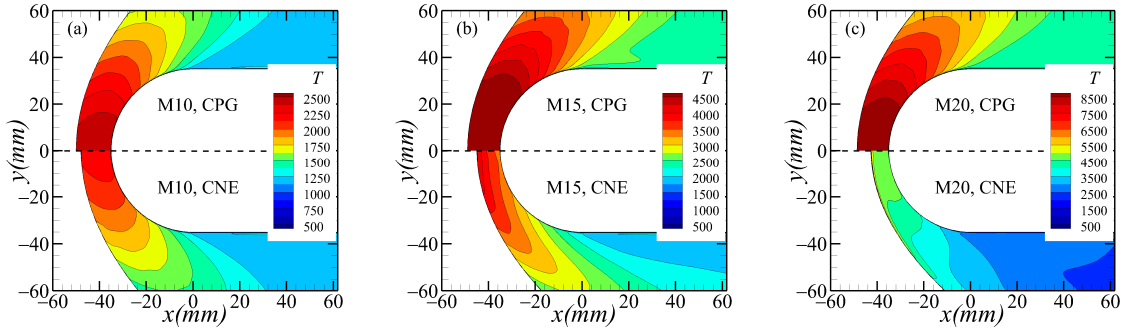

(**a**) Ma = 10 (**b**) Ma = 15 (**c**) Ma = 20

Figure 3. Temperature distribution around the nose region.

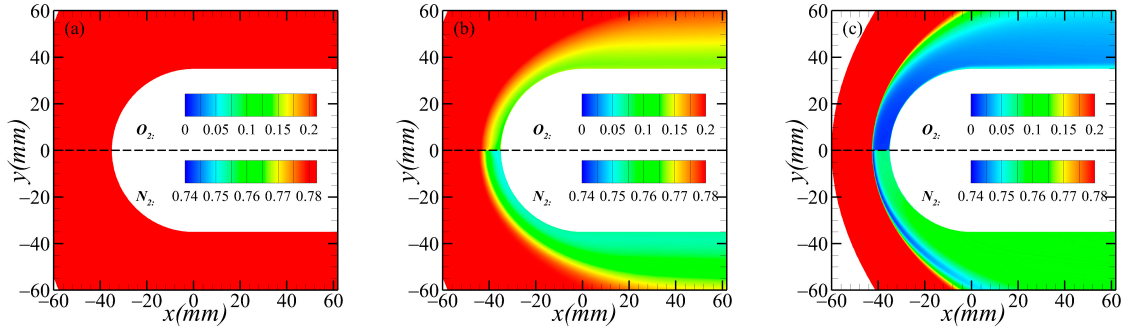

(**a**) Ma = 10 (**b**) Ma = 15 (**c**) Ma = 20

Figure 4. Oxygen/nitrogen mass fraction distribution around the nose region.

Figure 5 illustrates the temperature and velocity profiles in the boundary layer for various Mach numbers. It is apparent that the chemical nonequilibrium effect reduces both the temperature and velocity within the boundary layer, leading to modifications in the flow properties at the boundary layer's edge. The variation in flow characteristics at the boundary layer's edge can be attributed to changes in the shock wave intensity. As shown in Figure 6a, the shock angle for the CNE model in the downstream region significantly deviates from that of the CPG model. The post-shock parameters also exhibit variations because of the differing shockwave intensities between the two models.

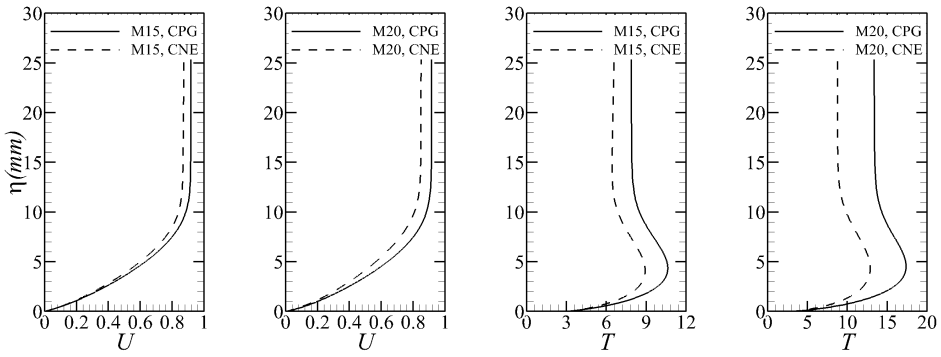

(**a**) (**b**) (**c**) (**d**)

Figure 5. Base flow profile: (**a**,**b**) velocity, (**c**,**d**) temperature.

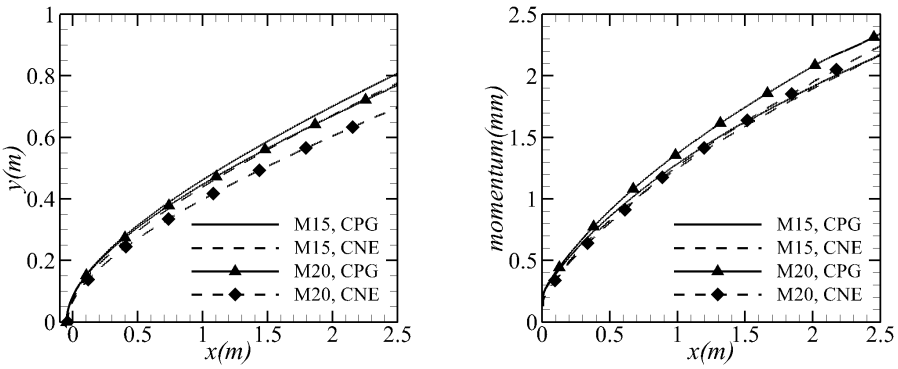

(**a**) (**b**)

Figure 6. Shockwave position (**a**) and the boundary layer momentum thickness (**b**).

Figure 6b shows the boundary layer momentum thickness, indicating that there is no noticeable difference in the momentum thicknesses for different gas models when the

Mach number is small. However, as the Mach number increases, the momentum thickness for the CNE model decreases noticeably. Some previous studies also considered real gas effects on boundary layer flow, but the wall conditions were mostly adiabatic. These studies discovered that chemical reactions contribute to a decreased wall temperature, exhibiting an influence similar to wall cooling. This study finds that chemical reactions cooled the flow within the boundary layer for isothermal walls, decreasing its thickness despite the constant wall temperature.

The unstable growth rate distributions for various Mach numbers and gas models are shown in Figure 7, including the second mode and stationary and traveling crossflow modes. The unstable frequency range and growth rate of the second mode appear to escalate, while the crossflow mode stabilizes with an increasing Mach number. As shown in Figure 7b–f, the chemical nonequilibrium effect further destabilizes the second mode and crossflow modes. The growth rate peaks for the CNE model are notably larger than those of the CPG model. When the Mach number reaches 15, the peak growth rate of the second mode significantly surpasses that of the crossflow mode.

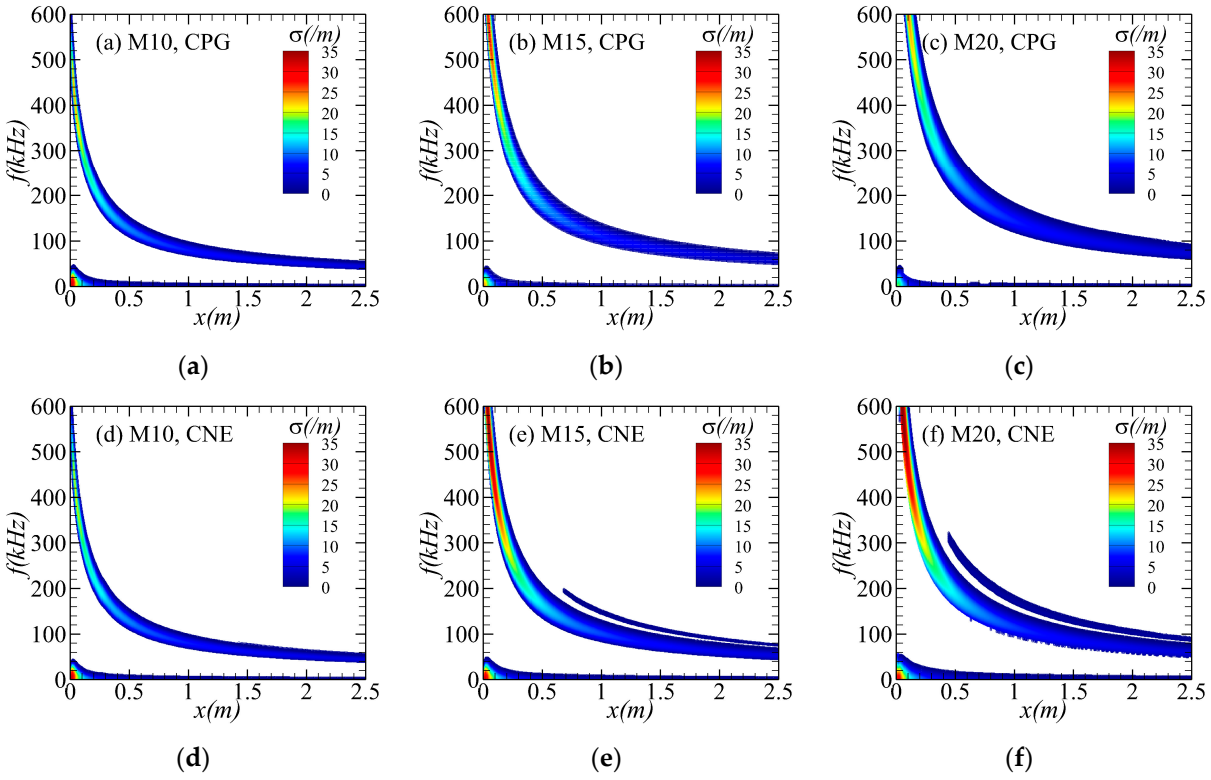

Figure 7. Growth rate distributions: (**a**) M10, CPG; (**b**) M15, CPG; (**c**) M20, CPG; (**d**) M10, CNE; (**e**) M15, CNE; (**f**) M20, CNE.

Figure 8 shows the N-factor envelope of the second and stationary crossflow modes for the CNE model at Ma = 20. While the second mode exhibits a higher peak growth rate at this point, its shorter integration path results in a smaller N-factor. By contrast, the stationary crossflow mode's longer growth path allows it to dominate downstream transitions.

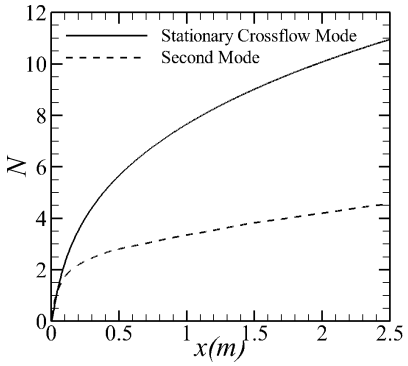

Figure 8. N-factor envelope (Ma = 20, CNE).

Figure 9 illustrates the N-factor of stationary crossflow modes at various Mach numbers. Figure 9a,b shows the N-factor envelope curves for the CPG and CNE models, respectively, while Figure 9c presents the N-factor at x = 2 m. As shown in Figure 9c, the N-factor decreases with increasing Mach number in the calorically perfect gas model. In other words, increasing the Mach number makes the stationary crossflow modes more stable, referred to as the Mach number effect.

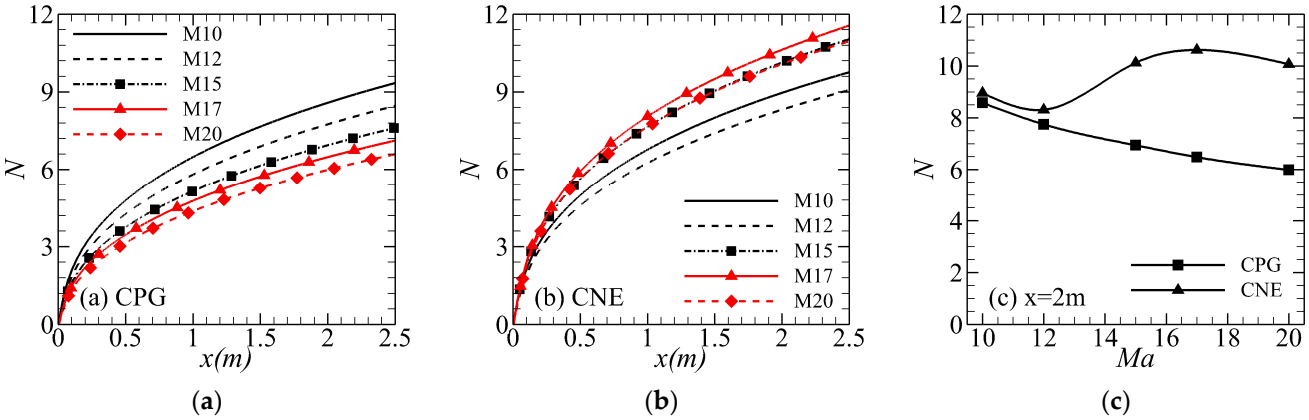

Figure 9. N-factor: (**a**,**b**) N-factor envelopes, (**c**) N-factor at x = 2 m.

Chemical nonequilibrium effects become non-negligible with increasing Mach number. The N-factor for the CNE model is significantly larger than that of the CPG model at the same Mach number, indicating that the chemical nonequilibrium effect further destabilizes the stationary crossflow modes. For the CNE model, a non-monotonic N-factor trend is observed as the Mach number increases. Initially, the N-factor decreases as the Mach number increases from 10 to 12. At this stage, the Mach number is relatively low, chemical nonequilibrium effects are weak, and the Mach number effects are dominant.

As the Mach number increases to 17, the influence of chemical nonequilibrium effects becomes substantial, resulting in an increase in the N-factor with rising Mach number. However, as the Mach number further increases to 20, the N-factor declines and approaches the value observed at Ma = 15. This phenomenon could be attributed to the Mach number effect's enhanced stabilizing impact on the stationary crossflow modes despite intensifying chemical nonequilibrium effects as the Mach number continues to rise. At this point, the Mach number effect regains dominance. In essence, the Mach number effect and the chemical nonequilibrium effect exhibit opposing influences on the stability of the stationary crossflow modes. These two effects compete, ultimately resulting in a non-monotonic variation of the N-factor in the CNE model.

3.2. Receptivity

We assume a Gaussian roughness distribution in the streamwise direction with a periodic distribution in the spanwise direction,

$$\varepsilon = he^{-\alpha(x-x_0)^2}\cos(\beta z) \tag{20}$$

where h is the roughness height, a is the shape factor, x_0 is the center position of the roughness, and β is the spanwise wavenumber. The specific parameters associated with these distributions are presented in Table 2, where δ is the scale of roughness in the streamwise direction.

Table 2. Roughness parameters.

Name	h (μm)	a	δ (m)	x_0 (m)
X35	40	0.025	0.035	0.35
X56	40	0.025	0.035	0.56

The typical roughness height is in the micron range. In this paper, the roughness height is about 1% of the boundary layer thickness, permitting the use of boundary compensation methods to address the small-scale roughness. Specifically, the roughness surface ($y = \varepsilon$) retains the no-slip and isothermal boundary conditions, while a first-order Taylor expansion is implemented at the original wall ($y = 0$), resulting in equivalent boundary conditions at the wall,

$$u' = -\varepsilon\frac{\partial u}{\partial y}(0),\ T' = T_w - \varepsilon\frac{\partial T}{\partial y}(0) \tag{21}$$

Figure 10 illustrates the stationary crossflow mode receptivity coefficients obtained using ALST for both gas models. With the CPG model, the receptivity coefficient increases with the Mach number. Conversely, the CNE model demonstrates a rapid decline in the receptivity coefficient as the Mach number increases. The receptivity coefficient variation with Mach number at β = 60 m^{-1} is depicted in Figure 10c. The receptivity coefficients from the CNE model are significantly smaller than those from the CPG model at the same Mach number, indicating that the chemical nonequilibrium effect significantly reduces the receptivity of the stationary crossflow modes. Figure 10c also presents the receptivity coefficients for both roughness distributions, showing that the receptivity coefficient increases when roughness is closer to the upstream.

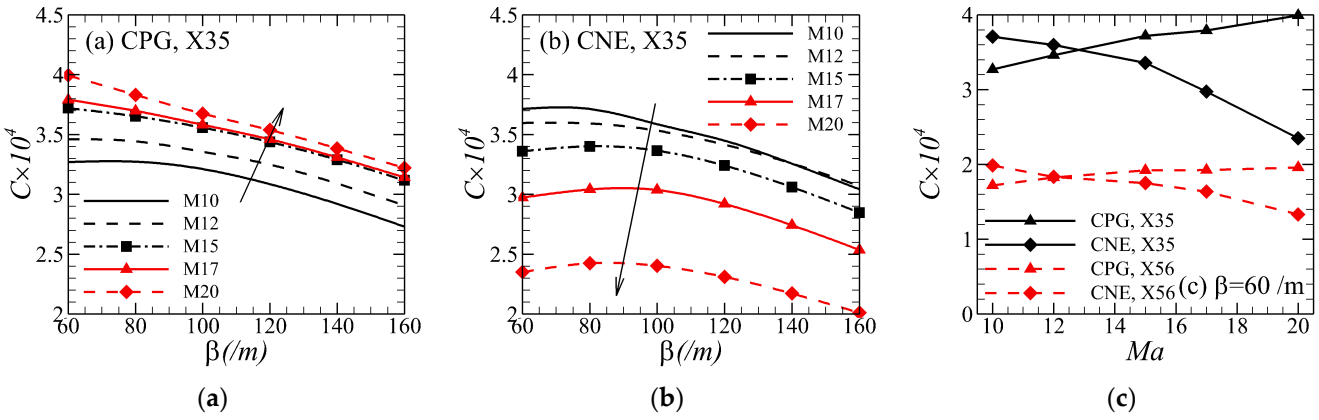

Figure 10. Receptivity coefficients for stationary crossflow modes: (**a**,**b**) receptivity coefficients with different spanwise wavenumbers, (**c**) receptivity coefficients with β = 60 m^{-1}.

It is worth noting that when Ma = 10–12, the receptivity coefficient of the CNE model is larger than that of the CPG model. However, based on the preceding analysis of the

base flow, it is evident that the boundary layer is mostly chemically frozen at low Mach numbers. Therefore, the observed increase in the receptivity coefficient for the CNE model is not attributable to chemical nonequilibrium effects. In addition to chemical reactions, the two gas models differ because the CPG model does not consider vibrational energy excitation, and their transport coefficients vary. However, exactly which effect leads to an increase in the stationary crossflow modes' receptivity coefficients at low Mach numbers requires further study.

Figure 11 shows the amplitude evolutions of stationary crossflow modes with different spanwise wavenumbers excited by roughness elements, and the amplitude envelope is also provided. Although the chemical nonequilibrium effect significantly reduces the receptivity of the stationary crossflow modes, it also results in a larger growth rate. At a Mach number of 20, the initial disturbance amplitude is low for the CNE model. However, upon exiting the excitation section, the disturbance amplitude rapidly increases, surpassing that of the CPG model, as shown in Figure 11b.

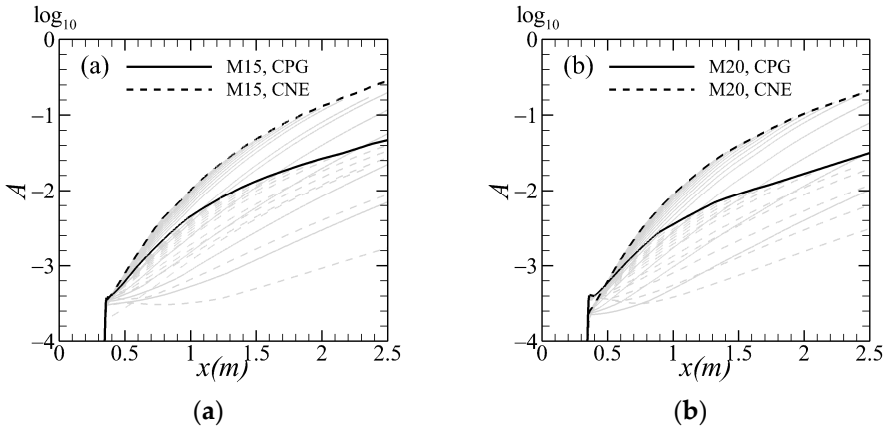

(**a**) (**b**)

Figure 11. Amplitude evolution of stationary crossflow modes: (**a**) Ma = 15, (**b**) Ma = 20.

Figure 12 shows the amplitude envelope for different Mach numbers. The trend of the amplitude envelope is similar to the N-factor envelope. For the CPG model, the amplitude gradually declines as the Mach number increases, whereas the CNE model exhibits a non-monotonic amplitude trend with increasing Mach number

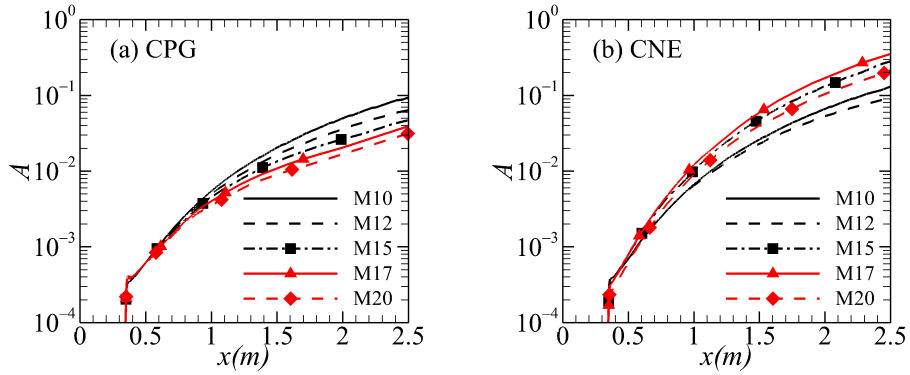

(**a**) (**b**)

Figure 12. Amplitude envelope of stationary crossflow modes: (**a**) CPG, (**b**) CNE.

Figure 13 illustrates the transition positions based on A = 5% and N = 8 predictions, with the latter not accounting for the effect of receptivity. Both methods show similar trends. The receptivity difference influences the transition position to a certain degree, but the more critical factors are the effects of Mach number and gas model on the stability of stationary crossflow modes. Chemical nonequilibrium effects appear for the blunt body swept flow

dominated by stationary crossflow modes as the Mach number increases, working in conjunction with the Mach number effect to cause two transition position reversals.

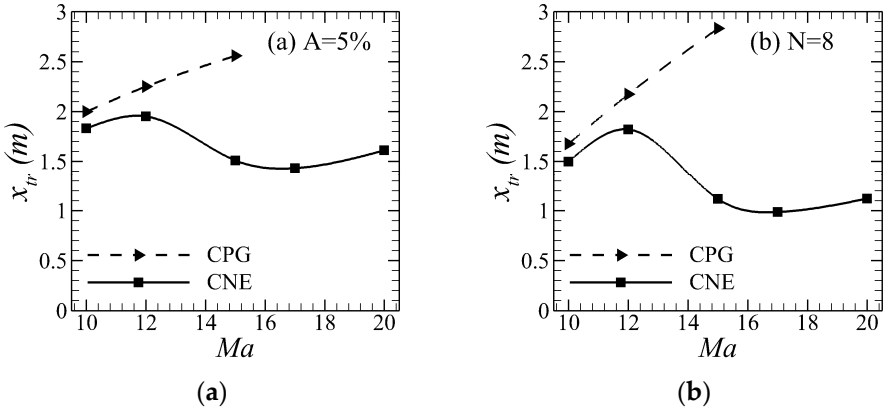

Figure 13. Transition position: (**a**) A = 5%, (**b**) N = 8.

At lower Mach numbers, the transition experiences a delay as the Mach number increases, followed by an advancement and subsequent delay in the transition position as the Mach number continues to rise. The CPG model predicts a transition position close to that of the CNE model at lower Mach numbers. However, when the Mach number exceeds 12, the CPG model predicts a transition position farther downstream, deviating significantly from the CNE model. This finding implies that it is crucial to account for the influence of chemical nonequilibrium effects when dealing with high-Mach-number conditions. Neglecting these effects may lead to erroneous predictions of the transition position.

4. Conclusions

This paper investigates the effects of the gas model and Mach number on the stability and receptivity of stationary crossflow modes using linear stability analysis (LST) and its adjoint (ALST). It was found that chemical nonequilibrium effects significantly alter the shock angle and, consequently, the flow quantities at the boundary layer's edge. As the Mach number increases, the second mode gradually becomes unstable while the crossflow mode stability improves. The growth rate of the second mode exceeds that of the crossflow mode after the Mach number exceeds a particular critical value. However, the stationary crossflow modes always dominate the transition because of their longer growth paths. Chemical nonequilibrium effects further destabilize the second and crossflow modes. The Mach number and chemical nonequilibrium effects have opposite effects on the stability of stationary crossflow modes. These two effects alternately dominate with increasing Mach number.

The stationary crossflow modes are excited by distributed roughness. The results indicate that the receptivity coefficients of stationary crossflow modes gradually increase with increasing Mach number, while the chemical nonequilibrium effect causes a significant decrease in the receptivity coefficients of stationary crossflow modes.

The combined influence of the Mach number and the gas model on receptivity and stability was examined by comparing disturbance amplitude envelopes. It was found that the difference in receptivity only affects the transition position to a certain extent. The effects of Mach number and gas model on the stability of the constant crossflow modes are more important. In a blunt body swept flow dominated by stationary crossflow modes, chemical nonequilibrium and Mach number effects combine to result in two reversals in the transition position. This study highlights the significant influence of real gas effects on the receptivity and stability of stationary crossflow modes. Specifically, it is necessary to consider the influence of chemical nonequilibrium effects at high Mach numbers to prevent incorrect predictions of the transition position.

Author Contributions: Conceptualization, Y.Y., J.L., and R.L.; methodology, J.L. and Z.H.; software, Z.H.; validation, Y.Y. and R.L.; formal analysis, Y.Y.; investigation, Y.Y. and R.L.; resources, J.L. and Z.H.; data curation Y.Y. and R.L.; writing—original draft preparation, Y.Y. and R.L.; writing—review and editing, Y.Y., Z.H. and J.L.; visualization, R.L.; project administration, Z.H. and J.L. All authors have read and agreed to the published version of the manuscript.

Funding: This research was funded by the State Key Laboratory of Aerodynamics Funding (Grant No. SKLA-20200103) and the National Natural Science Foundation of China (Grant Nos. 92271102, 12172252, 92052301 and 91952202).

Data Availability Statement: The data presented in this study can be obtained by e-mailing the corresponding author.

Conflicts of Interest: The authors declare no conflicts of interest.

Appendix A

In this paper, we employ two air chemical reaction models: the 5-species 5-reactions model [16] and the 11-species 21-reactions model [34]. Detailed chemical reaction equations are presented in Tables A1 and A2, while the corresponding parameters for reaction rates can be referenced from Refs. [16,34].

Table A1. 5-species 5-reactions model.

No.	Reactions
1	$O_2 + M_1 \Longleftrightarrow 2O + M_1$
2	$N_2 + M_1 \Longleftrightarrow 2N + M_1$
3	$NO + M_1 \Longleftrightarrow N + O + M_1$
4	$NO + O \Longleftrightarrow N + O_2$
5	$N_2 + O \Longleftrightarrow NO + N$

$M_1 = O_2,\ N_2,\ O,\ N,\ NO.$

Table A2. 11-species 21-reactions model.

No.	Reactions
1	$N_2 + M_1 \Longleftrightarrow 2N + M_1$
2	$O_2 + M_2 \Longleftrightarrow 2O + M_2$
3	$NO + M_2 \Longleftrightarrow N + O + M_2$
4	$NO + O \Longleftrightarrow O_2 + N$
5	$N_2 + O \Longleftrightarrow NO + N$
6	$N + O \Longleftrightarrow NO^+ + e^-$
7	$2O \Longleftrightarrow O_2^+ + e^-$
8	$2N \Longleftrightarrow N_2^+ + e^-$
9	$NO^+ + O \Longleftrightarrow N^+ + O_2$
10	$N^+ + N_2 \Longleftrightarrow N_2^+ + N$
11	$O_2^+ + N \Longleftrightarrow N^+ + O_2$
12	$O^+ + NO \Longleftrightarrow N^+ + O_2$
13	$O_2^+ + N_2 \Longleftrightarrow N_2^+ + O_2$
14	$O_2^+ + O \Longleftrightarrow O^+ + O_2$
15	$NO^+ + N \Longleftrightarrow O^+ + N_2$
16	$NO^+ + O_2 \Longleftrightarrow O_2^+ + NO$
17	$NO^+ + O \Longleftrightarrow O_2^+ + N$
18	$O^+ + N_2 \Longleftrightarrow N_2^+ + O$
19	$NO^+ + N \Longleftrightarrow N_2^+ + O$
20	$O + e^- \Longleftrightarrow O^+ + 2e^-$
21	$N + e^- \Longleftrightarrow N^+ + 2e^-$

$M_1 = O_2,\ N_2,\ O,\ N,\ NO,\ e^-,\ NO^+,\ O^+,\ N^+,\ O_2^+,\ N_2^+; M_2 = O_2,\ N_2,\ O,\ N,\ NO,\ NO^+,\ O^+,\ N^+,\ O_2^+,\ N_2^+.$

References

1. Morkovin, M.V.; Reshotko, E.; Herbert, T. Transition in open flow systems: A reassessment. *Bull. APS.* **1994**, *39*, 1882.

2. Goldstein, M.E.; Sockol, P.M.; Sanz, J. The evolution of Tollmien-Schlichting waves near a leading edge: Part 2. Numerical determination of amplitudes. *J. Fluid Mech.* **1983**, *129*, 443. [CrossRef]
3. Kerschen, E.J.; Choudhari, M.; Heinrich, R.A. Generation of boundary instability waves by acoustic and vortical freestream disturbances. In *Laminar-Turbulent Transition. International Union of Theoretical and Applied Mechanics*; Arnal, D., Michel, R., Eds.; Springer: Berlin/Heidelberg, Germany, 1990; pp. 477–488.
4. Hammerton, P.W.; Kerschen, E.J. Boundary-layer receptivity for a parabolic leading edge: Part 2. The small-Strouhal-number limit. *J. Fluid Mech.* **2000**, *353*, 205–220. [CrossRef]
5. Hammerton, P.W.; Kerschen, E.J. Effect of leading-edge geometry and aerodynamic loading on receptivity to acoustic disturbances. In *Laminar-Turbulent Transition. IUTAM Symposia*; Fasel, H.F., Saric, W.S., Eds.; Springer: Berlin/Heidelberg, Germany, 2000; pp. 37–42.
6. Fedorov, A. Transition and Stability of High-Speed Boundary Layers. *Annu. Rev. Fluid Mech.* **2011**, *43*, 79–95. [CrossRef]
7. Zhong, X.; Wang, X. Direct Numerical Simulation on the Receptivity, Instability, and Transition of Hypersonic Boundary Layers. *Annu. Rev. Fluid Mech.* **2012**, *44*, 527–561. [CrossRef]
8. Goldstein, M.E. Scattering of acoustic waves into Tollmien-Schlichting waves by small streamwise variations in surface geometry. *J. Fluid Mech.* **1985**, *154*, 509–529. [CrossRef]
9. Choudhari, M.; Kerschen, E. Instability wave patterns generated by interaction of sound waves with three-dimensional wall suction or roughness. *AIAA J.* **1990**, *90*, 0119.
10. Crouch, J.D. Localized receptivity of boundary layers. *Phys. Fluids* **1992**, *4*, 1408. [CrossRef]
11. Ruban, A.I.; Kravtsova, M.A. Generation of steady longitudinal vortices in hypersonic boundary layer. *J. Fluid Mech.* **2013**, *729*, 702–731. [CrossRef]
12. Duan, L.; Wang, X.; Zhong, X.A. High Order Cut-Cell Method for Numerical Simulation of Hypersonic-Boundary Transition with Arbitrary Surface Roughness. In Proceedings of the 47th AIAA Aerospace Sciences Meeting including The New Horizons Forum and Aerospace Exposition, Orlando, FL, USA, 5–8 January 2009.
13. Tempelmann, D.; Schrader, L.U.; Hanifi, A. Swept wing boundary-layer receptivity to localized surface roughness. *J. Fluid Mech.* **2012**, *711*, 516–544. [CrossRef]
14. Wang, Y.; Li, Y.; Liu, J. On the receptivity of surface plasma actuation in high-speed boundary layers. *Phys. Fluids* **2020**, *32*, 094102. [CrossRef]
15. Xi, Y.; Ren, J.; Wang, L. Receptivity and stability of hypersonic leading-edge sweep flows around a blunt body. *J. Fluid Mech.* **2021**, *916*, R2. [CrossRef]
16. Anderson, J.D., Jr. *Hypersonic and High Temperature Gas Dynamics*, 2nd ed.; AIAA: Reston, VA, USA, 2006.
17. Malik, M.R. *Stability Theory for Chemically Reacting Flows*; Springer: Berlin/Heidelberg, Germany, 1990.
18. Malik, M.R.; Anderson, E.C. Real gas effects on hypersonic boundary-layer stability. *Phys. Fluids* **1991**, *3*, 803–821. [CrossRef]
19. Stuckert, G.; Reed, H.L. Linear disturbances in hypersonic, chemically reacting shock layers. *AIAA J.* **1994**, *32*, 1384–1393. [CrossRef]
20. Chang, C.L.; Vinh, H.; Malik, M. Hypersonic boundary-layer stability with chemical reactions using PSE. In Proceedings of the 28th Fluid Dynamics Conference, Snowmass Village, CO, USA, 29 June–2 July 1997.
21. Franko, K.; Maccormack, R.; Lele, S. Effects of Chemistry Modeling on Hypersonic Boundary Layer Linear Stability Prediction. In Proceedings of the 40th Fluid Dynamics Conference and Exhibit, Chicago, IL, USA, 28 June–1 July 2010.
22. Fernando, M.M.; Pinna, F.; Beyak, E.S. Diffusion and chemical non-equilibrium effects on hypersonic boundary-layer stability. In Proceedings of the 2018 AIAA Aerospace Sciences Meeting, Kissimmee, FL, USA, 8–12 January 2018.
23. Candier, G.V.; MacCormack, R.W. The Computation of Hypersonic Ionized Flows in Chemical and Thermal Nonequilibrium. In Proceedings of the 26th Aerospace Sciences Meeting, Reno, NV, USA, 11–14 January 1988; pp. 88–511.
24. Grantham, W.L. *Flight Results of A 25000 Foot Per Second Reentry Experiment Using Microwave Reflectometers to Measure Plasma Electron Density and Standoff Distance*; NASA Technical Note; National Aeronautics and Space Administration: Washington, DC, USA, 1970; p. 6062.
25. Fernando, M.M.; Beyak, E.S.; Pinna, F. High-enthalpy models for boundary-layer stability and transition. *Phys. Fluids* **2019**, *31*, 44101.
26. Han, Y.; Cao, W. Interaction between Mack second mode and radiation mode in high-enthalpy boundary layers. *Phys. Fluids* **2022**, *34*, 094109. [CrossRef]
27. Knisely, C.P.; Zhong, X. Significant Supersonic Modes and the Wall Temperature Effect in Hypersonic Boundary Layers. *AIAA J.* **2019**, *57*, 1552–1566. [CrossRef]
28. Mortensen, C. Toward an understanding of supersonic modes in boundary-layer transition for hypersonic flow over blunt cones. *J. Fluid Mech.* **2018**, *846*, 789–814. [CrossRef]
29. Marxen, O.; Iaccarino, G.; Magin, T.E. Direct numerical simulations of hypersonic boundary-layer transition with finite-rate chemistry. *J. Fluid Mech.* **2014**, *755*, 35–49. [CrossRef]
30. Zanus, L.; Pinna, F. Stability Analysis of Hypersonic Flows in Local Thermodynamic Equilibrium Conditions by Means of Nonlinear PSE. In Proceedings of the 2018 Fluid Dynamics Conference, Atlanta, GA, USA, 25 June 2018.
31. Chen, X.; Wang, L.; Fu, S. Secondary instability of the hypersonic high-enthalpy boundary layers with thermal–chemical nonequilibrium effects. *Phys. Fluids* **2021**, *33*, 034132. [CrossRef]

32. Thompson, R.A.; Lee, K.P.; Gupta, R.N. *Computer Codes for the Evaluation of Thermodynamic Properties, Transport Properties, and Equilibrium Constants of an 11-Species Air Model*; NASA Technical Memorandum; National Aeronautics and Space Administration, Langley Research Center: Hampton, VA, USA, 1990; p. 102601.
33. Gupta, R.N.; Yos, J.M.; Thompson, R.A. *A Review of Reaction Rates and Thermodynamic and Transport Properties for the 11-Species Air Model for Chemical and Thermal Nonequilibrium Calculations to 30000 K*; NASA Reference Publication; National Aeronautics and Space Administration, Office of Management, Scientific and Technical Information Division: Washington, DC, USA, 1990; p. 1232.
34. Park, C. Assessment of Two-Temperature Kinetic Model for Ionizing Air. In Proceedings of the AIAA, Thermophysics Conference, 22nd, Honolulu, HI, USA, 8–10 June 1987; pp. 87–1574.